Title

Chemical and Structural Diversity of Hybrid Layered Double Perovskite Halides

Journal

Journal of the American Chemical Society, 141(48)

ISSN

0002-7863 1520-5126

Authors

Mao, Lingling
Teicher, Samuel M. L
Stoumpos, Constantinos C
et al.

Publication Date

2019-11-07

DOI

10.1021/jacs.9b09945

Peer reviewed

Chemical and Structural Diversity of Hybrid Layered Double Perovskite Halides

Lingling Mao[1], Samuel M. L. Teicher[1], Constantinos C. Stoumpos[2], Rhys M. Kennard[1], Ryan A. DeCrescent[3], Guang Wu[4], Jon A. Schuller[5], Michael L. Chabinyc[1], Anthony K. Cheetham[1,6*] and Ram Seshadri[1,4*]

[1]Materials Research Laboratory and Materials Department, [3]Department of Physics, [4]Department of Chemistry and Biochemistry, [5]Department of Electrical and Computer Engineering, University of California, Santa Barbara, California 93106, United States

[2]Department of Materials Science and Technology, University of Crete, Vassilika Voutes GR-700 13 Heraklion, Greece

[6]Department of Materials Science & Engineering, National University of Singapore 9 Engineering Drive 1, Singapore 117576, Singapore

ABSTRACT: Hybrid halide double perovskites are a class of compounds attracting growing interest because of their richness of structure and property. Two-dimensional (2D) derivatives of hybrid double perovskites are formed by the incorporation of organic spacer cations into three-dimensional (3D) double perovskites. Here, we report a series of seven new layered double perovskite halides with propylammonium (PA), octylammonium (OCA), and 1,4-butydiammonium (BDA) cations. The general formulae of the compounds are $A_mM^{I}M^{III}X_8$ (single-layered Ruddlesden-Popper with $m = 4$ and A = PA or OCA, and single-layered Dion-Jacobson with $m = 2$ and A = BDA, M^{I} = Ag, M^{III} = In or Bi, X = Cl or Br) and $PA_2CsM^{I}M^{III}Br_7$ (bi-layered, with M^{I} = Ag, M^{III} = In or Bi). These families of compounds demonstrate great versatility, with tunable layer thickness, the ability to vary the interlayer spacing, and the ability to selectively tune the band gap by varying the M^{I} and M^{III} cations along with the halide anions. The band gap of the single-layered materials varies from 2.41 eV for $PA_4AgBiBr_8$ to 3.96 eV for $PA_4AgInCl_8$. Photoluminescent emission spectra of the layered double perovskites at low-temperature (100 K) are reported, and density functional theory electronic structure calculations are presented to understand the nature of the band gap evolution. The development of new structural and compositions in layered double perovskite halides enhances the understanding of structure-property relations in this important family.

INTRODUCTION

Hybrid organic-inorganic halide perovskite materials have sparked widespread interest due to the richness of their optoelectronic properties.[1-5] The three-dimensional (3D) halide perovskites are established materials that show high power conversion efficiencies in solar cells[6,7] and high external quantum efficiencies in light-emitting diodes.[8-11] The general formula of the 3D hybrid halide perovskites is AMX_3, where A is a small organic cation such as methylammonium (MA^+), formamidinium (FA^+); M is Ge^{2+}, Sn^{2+}, or Pb^{2+}, and X is a halide.[12] Double perovskites are obtained by doubling the formula, using alternating 1+ and 3+ on the M site instead of a 2+ cation metals. The resulting 3D structures have the general formula $A_2M^{I}M^{III}X_6$[13] (displayed in Figure 1). While the A site cation stems from a similar pool as found in AMX_3 perovskites, M^{I} and M^{III} offer a wide range of tunability, from Na^+, K^+, Cu^+, Ag^+, Au^+, for M^{I} and, from Y^{3+}, Gd^{3+}, Au^{3+}, In^{3+}, Tl^{3+}, Sb^{3+}, Bi^{3+}, for M^{III}.[14-26] Double perovskites with three-dimensionally linked octahedra have demonstrated interesting physical properties and desirable "lead-free" compositions,[27] which make them a unique class of hybrid materials. Vacancy-ordered double perovskites[28,29] can also be formed with a 4+ metal alternating with a vacancy as in Cs_2SnI_6.[30]

By tuning the size and nature of the A cation (or combinations of cations) in 3D AMX_3 perovskites, distinct classes of hybrid 2D layered perovskites can be obtained, including the so-called Ruddlesden-Popper series[31,32] and the Dion-Jacobson series[33,34] (displayed in Figure 1). In a similar vein, the introduction of appropriate large organic spacing cations[35] has recently yielded hybrid layered double perovskite halides (schematically represented in Figure 1). The first example was obtained by incorporating butylammonium (BA) cations into $Cs_2AgBiBr_6$ resulting in two new structures, $BA_4AgBiBr_8$ and $BA_2CsAgBiBr_7$.[36] High pressure studies based on $BA_4AgBiBr_8$[37] and using $BA_2CsAgBiBr_7$[38] for X-ray detection have just been reported. An iodide-based 2D double perovskite $[AE2T]_2AgBiI_8$ (AE2T = 5,5'-diylbis(amino-ethyl)-[2,2'-bithiophene]) has also been recently reported, with an optical band gap of 2.00 eV.[39] Hydrothermal synthesis and structure of the compounds $(C_6H_{16}N_2)_2AgBiI_8{\cdot}H_2O$ and $(C_6H_{16}N_2)_2CuBiI_8{\cdot}0.5H_2O$ [$C_6H_{14}N_2$ = 1,4- cyclohexane-diamine] have also been reported recently.[40]

With the aim of evaluating the chemical and structural versatility of hybrid layered double perovskite halides, and to gain insight into structure-property relations, we demonstrate that a large family of cation-ordered hybrid double-perovskite halides can be obtained through the judicious selection of a range of organic and M cations, and halide anions. New members of hy-

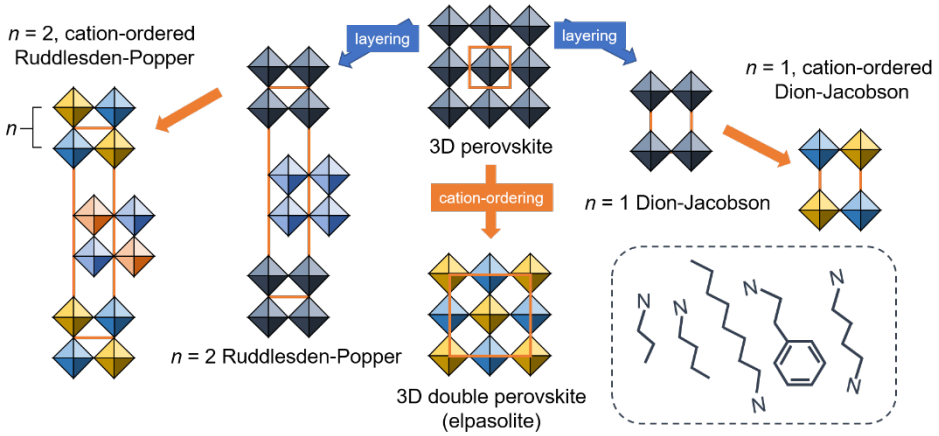

Figure 1. Schematic illustration of the evolution of the 3D perovskite structure to 2D layered double perovskites. For clarity, the *A* cations are not depicted. Cation ordering in the *M* site of AMX_3 perovskite yields the 3D double perovskite structure, and the insertion of spacer cations allows the layering. The two main classes of layered structures are the Ruddlesden-Popper type, depicted on the left as the $n = 2$ member, and the Dion-Jacobson type, shown on the right as the $n = 1$ member. A few sample organic spacer cations are depicted in the inset.

brid cation-ordered Ruddlesden-Popper (RP) and Dion-Jacobson (DJ) phases are reported. First we describe the successful preparation of 2D derivatives $PA_4AgInCl_8$ and $PA_4AgBiBr_8$ where PA= propylammonium. These could be thought of as being derived from the known 3D double perovskites $Cs_2AgInCl_6$ and $Cs_2AgBiBr_6$. Alternatively, these could be seen as being derived from the $n = 1$ Ruddlesden-Popper phase PA_2PbX_4, with Pb^{2+} being replaced by alternating Ag^+ and In^{3+}/Bi^{3+} To our surprise, although $Cs_2AgInBr_6$ has not been reported and does not seem to form directly through solution methods, the layered product $PA_4AgInBr_8$ does form, and is structurally analogous to $PA_4AgBiBr_8$. The single-layered ($n = 1$) series is further expanded by using the longer octylammonium (OCA) cation, forming $OCA_4AgBiBr_8$. The use of a dication, 1,4-butanediammonium (BDA) yields the $n = 1$ Dion-Jacobson phase $BDA_2AgBiBr_8$. Building up the layer thickness is realized up to $n = 2$, with the successful preparation of $PA_2CsAgBiBr_7$ and $PA_2CsAgIn_{0.5}Bi_{0.5}Br_7$. The optical properties are highly tunable, through varying the layer thickness, increasing the length of the organic spacer, changing the halide (from Cl^- to Br^-) and alloying the metal (M^{III}). With the flexible toolbox described above, we have discovered seven new hybrid layered double perovskite halides with tunable properties.

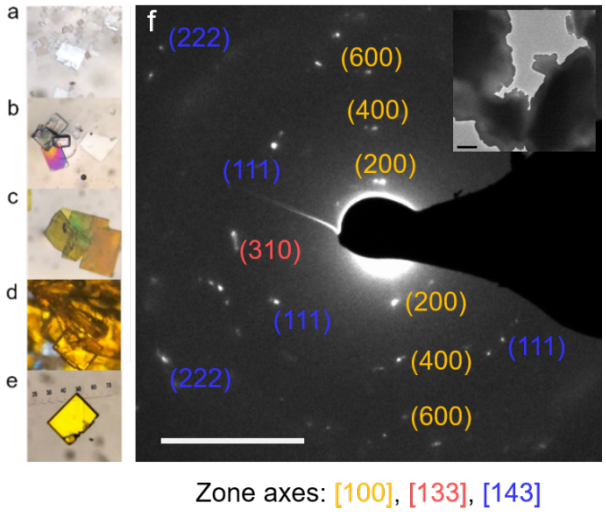

Figure 2. Optical microscope images of (a) $PA_4AgInCl_8$, (b) $PA_4AgInBr_8$ (colorless, the purple comes from interference effect), (c) $PA_4AgBiBr_8$, (d) $PA_2CsAgBiBr_7$ and (e) $PA_2CsAgBi_{0.5}In_{0.5}Br_7$. (f) Selected Area Electron Diffraction (SAED) of fragments of $PA_4AgBiBr_8$, showing spots corresponding to the labelled *d*-spacings, with real-space Transmission Electron Microscopy (TEM) image of fragments inset. Scale bars: 2 nm^{-1} for the SAED image and 1 μm for the real-space image. inset, showing *d*-spacing of 3.1 Å.

RESULTS AND DISCUSSION

Synthesis. The synthesis of the 2D double perovskites involves the dissolution of the metal precursors in concentrated hydrohalic acid media followed by the precipitation of the desired crystals upon addition of the bulky alkylammonium cation. All as-formed crystals have a signature plate-like morphology with varying color, as seen in Figure 2a-e. The general principle remains similar to the one used for common 2D perovskites, although due to the relatively lower solubility of the material, unique processes are required, such as the filtration of some insoluble precipitates to afford clear solutions that allow for the isolation of compositionally pure compounds (for more details see Methods). Direct visualization of the structure of a $PA_4AgBiBr_8$ crystal was obtained via Transmission Electron Microscopy (TEM) and Selected Area Electron Diffraction (SAED) (Figure 2f), whereby analysis was performed on thin edges of fragments of *single-layered* crystals. The fragments were deposited onto TEM grids by crushing the crystals onto TEM grids with a razor blade, resulting in crystallites of different orientations being simultaneously imaged (for imaging conditions, see Methods section). An example of selected area electron diffraction analysis on such a fragment is shown in Figure 2f, with the real space image of a selected area shown in the inset. The fragments are primarily oriented along the [100] zone axis, as evidenced by strong diffraction from (200), (400), and (600) *d*-spacings (in yellow) with some contribution from the [133] and [143] zone axes.

Crystal structures. The general structures of these layered double perovskites are similar to the traditional layered perovskite, with the distinct difference that the metal-centered octahedra

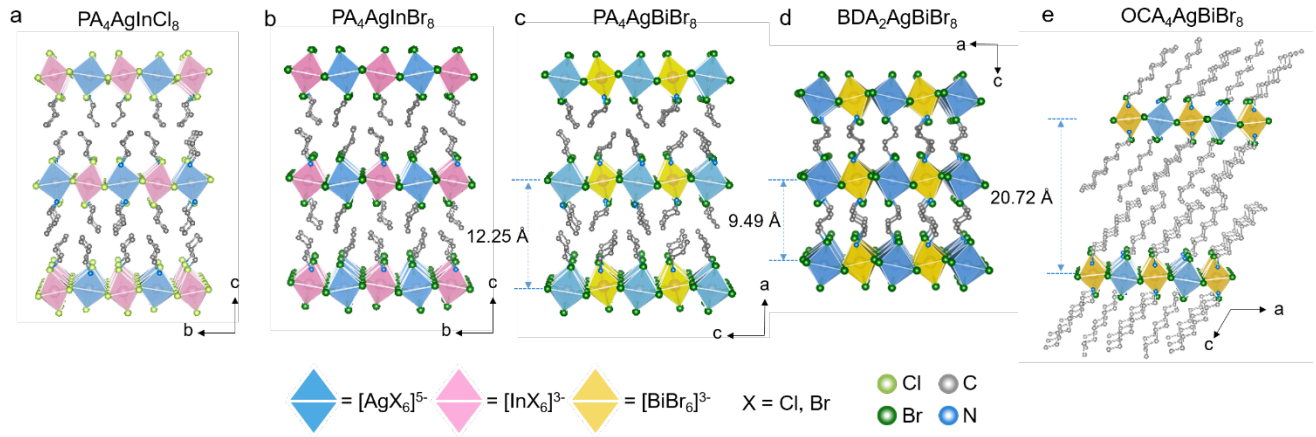

Figure 3. Crystal structures of the single-layered compounds (a) $PA_4AgInCl_8$, (b) $PA_4AgInBr_8$, (c) $PA_4AgBiBr_8$, (d) $BDA_4AgBiBr_8$ and (e) $OCA_4AgBiBr_8$. Hydrogens are omitted for clarity.

are made from alternating M^{I} and M^{III} (M^{I} = Ag, M^{III} = In, Bi). The layered double perovskites have general formulae of A_m-$M^{I}M^{III}X_8$ and $PA_2Cs M^{I}M^{III}Br_7$. The alternating metal arrangement of the single-layered materials studied here is illustrated in Figure 3, where the layers are composed of corner-sharing Ag/In-centered (blue/pink) and Ag/Bi-centered (blue/yellow) octahedra. The layers follow the (100)-orientation, which is the most common type found in the layered perovskites.[4,41] We started with a short akylammonium cation, propylammonium (PA) as the template, then continued to expand to octylammonium (OCA) and the di-cation 1,4-butanediammonium (BDA). Variations on the M^{III} and X parts have been carried out: In and Bi for M^{III}, and Cl and Br for the halide, as seen in Figure 1. Efforts have also been made to synthesize higher layer thickness, however, we were successful only up to two layers. Detailed crystallographic data and refinement details are listed in Tables 1 and 2.

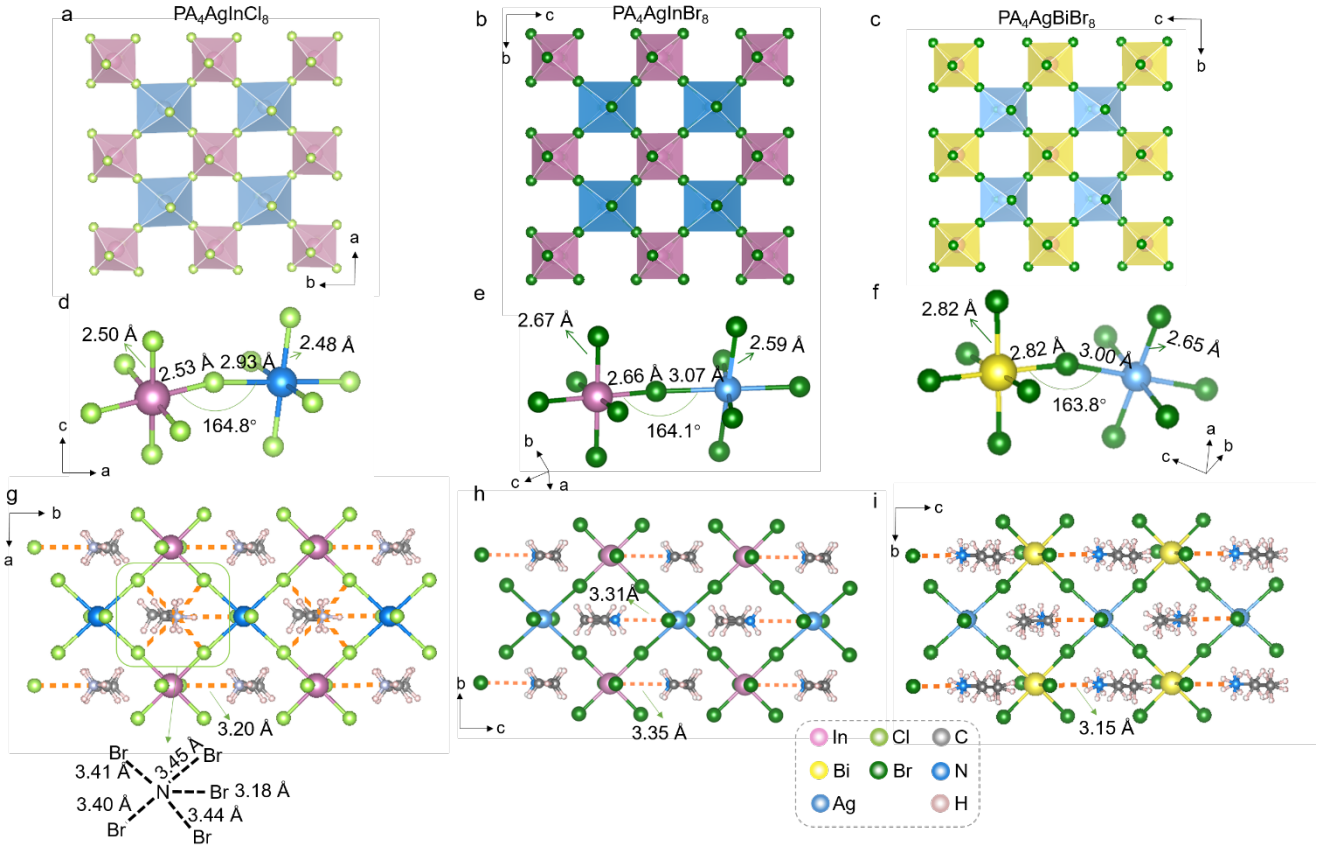

Figure 4. Top-down view of the layers in (a) $PA_4AgInCl_8$, (b) $PA_4AgInBr_8$ and (c) $PA_4AgBiBr_8$. Local bonding environment of (d) $PA_4AgInCl_8$, (e) $PA_4AgInBr_8$ and (f) $PA_4AgBiBr_8$. Hydrogen bonding network of (g) $PA_4AgInCl_8$ (H-bond cutoff 3.45 Å), (h) $PA_4AgInBr_8$ (H-bond cutoff 3.50 Å), and (i) $PA_4AgBiBr_8$ (H-bond cutoff 3.50 Å).

Table 1. Crystal Data and Structure Refinement for $PA_4AgInCl_8$, $PA_4AgInBr_8$ and $PA_4AgBiBr_8$ at 293K.

Compound	$PA_4AgInCl_8$[1]	$PA_4AgInBr_8$[2]	$PA_4AgBiBr_8$[3]
Empirical formula	$(CH_3(CH_2)_2NH_3)_4AgInCl_8$	$(CH_3(CH_2)_2NH_3)_4AgInBr_8$	$(CH_3(CH_2)_2NH_3)_4AgBiBr_8$
Crystal system	Triclinic	Monoclinic	Monoclinic
Space group	$P\bar{1}$	*C2/m*	*C2/m*
Unit cell dimensions	a = 7.454(3) Å, α = 90.141(10)° b = 7.866(3) Å, β = 89.992(10)° c = 24.629(8) Å, γ = 90.049(11)°	a = 24.5633(13) Å, b = 7.7838(4) Å, c = 8.2501(4) Å, β = 90.091(2)°	a = 24.503(7) Å, b = 7.964(2) Å, c = 8.384(2) Å, β = 90.045(9)°
Volume	1444.0(8) Å^3	1577.38(14) Å^3	1636.0(8) Å^3
Z	2	2	2
Density (calculated)	1.717 g/cm^3	2.321 g/cm^3	2.429 g/cm^3
Absorption coefficient	2.224 mm^{-1}	11.491 mm^{-1}	15.746 mm^{-1}
F(000)	744	1032	1100
θ range for data collection	0.827 to 27.763°	2.47 to 31.74°	1.662 to 26.467°
Index ranges	-9<=h<=8, -8<=k<=9, -31<=l<=31	-36<=h<=36, -11<=k<=11, -12<=l<=12	-30<=h<=30, -8<=k<=9, -10<=l<=8
Reflections collected	9706	41147	5285
Independent reflections	5690 [R_{int} = 0.0442]	2845 [R_{int} = 0.0376]	1769 [R_{int} = 0.0568]
Completeness to θ = 24.868°	98.7%	100%	97.2%
Refinement method		Full-matrix least-squares on F^2	
Data / restraints / parameters	5690 / 0 / 157	2845 / 10 / 54	1769 / 10 / 53
Final R indices [I > 2σ(I)]	R_{obs} = 0.0760, wR_{obs} = 0.1955	R_{obs} = 0.0496, wR_{obs} = 0.1457	R_{obs} = 0.0956, wR_{obs} = 0.2648
R indices [all data]	R_{all} = 0.1952, wR_{all} = 0.2637	R_{all} = 0.0661, wR_{all} = 0.1472	R_{all} = 0.1381, wR_{all} = 0.2787
Largest diff. peak and hole	1.484 and -1.773 e·Å^{-3}	3.06 and -1.30 e·Å^{-3}	1.581 and -1.705 e·Å^{-3}

[1] $R = \Sigma||F_o|-|F_c|| / \Sigma|F_o|$, $wR = \{\Sigma[w(|F_o|^2 - |F_c|^2)^2] / \Sigma[w(|F_o|^4)]\}^{1/2}$ and $w=1/[\sigma^2(Fo^2)+(0.1245P)^2]$ where $P=(Fo^2+2Fc^2)/3$

[2] $R = \Sigma||F_o|-|F_c|| / \Sigma|F_o|$, $wR = \{\Sigma[w(|F_o|^2 - |F_c|^2)^2] / \Sigma[w(|F_o|^4)]\}^{1/2}$ and $w=1/[\sigma^2(Fo^2)+(0.1025P)^2+20.8371P]$ where $P=(Fo^2+2Fc^2)/3$

[3] $R = \Sigma||F_o|-|F_c|| / \Sigma|F_o|$, $wR = \{\Sigma[w(|F_o|^2 - |F_c|^2)^2] / \Sigma[w(|F_o|^4)]\}^{1/2}$ and $w=1/[\sigma^2(Fo^2)+(0.0843P)^2+136.0832P]$ where $P=(Fo^2+2Fc^2)/3$

Propylammonium cations were used to separate the 3D parent structure of $Cs_2AgInCl_6$ and form the Ruddlesden-Popper (RP) type layered perovskite, $PA_4AgInCl_8$, as shown in Figure 3a. $PA_4AgInCl_8$ crystallizes in the triclinic space group $p\bar{\mathbf{1}}$. Ag^I and In^{III} occupy distinct metal sites, which can be clearly distinguished by the octahedral environments. The In-Cl bond lengths (2.50 Å and 2.53 Å) are much shorter and more uniform compared with the Ag-Cl bonds (2.48 Å and 2.93 Å) in Figure 4d. Compared to the uniform Ag-Cl bond length in the 3D $Cs_2AgInCl_6$ structure (2.73 Å), the 2D material show a large deviation of the equatorial (2.93 Å) and axial (2.48 Å) Ag-Cl bond lengths. The two short axial bonds are situated in the positions without In connections (perpendicular to the layers). The extensive hydrogen bonding network between the NH_3^+ group and Cl is illustrated in Figure 4g, where the cutoff of the N···Cl distance is 3.45 Å. Amongst the hydrogen bonds (~3.40 Å),[42] those between nitrogen and terminal Cl are the strongest (3.18 Å and 3.20 Å, Figure 4g).

The bromide analogue $PA_4AgInBr_8$ crystallizes in the monoclinic space group *C2/m.* The Ag and In sites are fully resolved, unlike the recently reported structure $[AE2T]_2AgBiI_8$ (AE2T = 5,5′-diylbis(aminoethyl)-[2,2′-bithiophene]), where Bi and Ag, as well as the bridging iodine, have site disorders.[39] The In-Br bonds have consistent lengths of 2.66 Å and 2.67 Å , whereas the $[AgBr_6]^{5-}$ octahedron still again has compressed octahedral geometry, with elongated equatorial Ag-Br bonds (3.07 Å) and short axial Ag-Br bonds (2.59 Å) (Figure 4e). The H-bonds are even weaker than in the Ag/Br system, as seen in Figure 4h,

where the strongest H-bonds are between nitrogen and the terminal Br (3.31 Å and 3.35 Å). With the same organic spacing cation PA, the difference in the *M*-X-Ag angles ($M = In^{3+}$, Bi^{3+}, X = Cl, Br) are quite small, 164.8˚, 164.1˚ and 163.8˚, respectively.

Table 2. Crystal Data and Structure Refinement for $BDA_2AgBiBr_8$ $OCA_4AgBiBr_8$, $PA_2CsAgBiBr_7$, and $PA_2CsAgBi_{0.5}In_{0.5}Br_7$ at 293K.

Compound	$BDA_2AgBiBr_8$[1]	$OCA_4AgBiBr_8$[2]	$PA_2CsAgBiBr_7$[3]	$PA_2CsAgIn_{0.5}Bi_{0.5}Br_7$[4]
Empirical formula	$(NH_3(CH_2)_4NH_3)_2AgBiBr_8$	$(CH_3(CH_2)_7NH_3)_4AgBiBr_8$	$(CH_3(CH_2)_2NH_3)_2CsAgBiBr_7$	$(CH_3(CH_2)_2NH_3)_2CsAgBi_{0.52}In_{0.48}Br_7$
Crystal system	Triclinic	Monoclinic	Monoclinic	Monoclinic
Space group	$P\bar{1}$	$P2/m$	$P2_1/m$	$P2_1/m$
Unit cell dimensions	a = 8.1018(3) Å, α = 101.1960(10)° b = 8.2433(3) Å, β = 92.055(2)° c = 9.6813(4) Å, γ = 90.3960(10)°	a = 8.2024(7) Å, b = 8.1797(6) Å, c = 21.1217(18) Å, β = 101.195(3)°	a = 8.053(4) Å, b = 7.997(3) Å, c = 18.536(8) Å, β = 102.503(11)°	a = 8.008(10) Å, b = 7.877(9) Å, c = 18.310(2) Å, β = 102.60(3)°
Volume	633.79(4) $Å^3$	1390.2(2) $Å^3$	1165.5(9) $Å^3$	1127(2) $Å^3$
Z	1	1	2	2
Density (calculated)	2.978 g/cm^3	1.764	3.218 g/cm^3	3.194 g/cm^3
Absorption coefficient	20.314 mm^{-1}	9.284 mm^{-1}	21.907 mm^{-1}	19.398 mm^{-1}
F(000)	514	710.0	1000	967
θ range for data collection	2.516 to 30.594°	2.490 to 26.660°	1.125 to 25.678°	2.279 to 24.868°
Index ranges	-11<=h<=11, -11<=k<=11, -13<=l<=13	-11<=h<=11, -11<=k<=11, -26<=l<=26	-9<=h<=4, -9<=k<=9, -20<=l<=22	-9<=h<=9, -7<=k<=9, -19<=l<=21
Reflections collected	20023	40227	4810	4216
Independent reflections	3872 [R_{int} = 0.0555]	2702 [R_{int} = 0.0694]	2138 [R_{int} = 0.1009]	2092 [R_{int} = 0.0740]
Completeness to θ = 24.868°	99.4%	85.5%	92.4%	98.4%
Refinement method			Full-matrix least-squares on F^2	
Data / restraints / parameters	3872 / 0 / 105	2702 / 31 / 69	2138 / 13 / 78	2092 / 13 / 78
Final R indices [I > 2σ(I)]	R_{obs} = 0.0421, wR_{obs} = 0.1140	R_{obs} = 0.0919, wR_{obs} = 0.2714	R_{obs} = 0.1304, wR_{obs} = 0.2742	R_{obs} = 0.1313, wR_{obs} = 0.2580
R indices [all data]	R_{all} = 0.0445, wR_{all} = 0.1162	R_{all} = 0.1223, wR_{all} = 0.2752	R_{all} = 0.2065, wR_{all} = 0.3171	R_{all} = 0.1908, wR_{all} = 0.2801
Largest diff. peak and hole	4.539 and -2.316 e·$Å^{-3}$	2.93 and -1.48 e·$Å^{-3}$	5.786 and -4.368 e·$Å^{-3}$	3.276 and -4.440 e·$Å^{-3}$

[1] $R = \Sigma||F_o|-|F_c|| / \Sigma|F_o|$, $wR = \{\Sigma[w(|F_o|^2 - |F_c|^2)^2] / \Sigma[w(|F_o|^4)]\}^{1/2}$ and $w=1/[\sigma^2(Fo^2)+(0.0661P)^2+2.3572P]$ where $P=(Fo^2+2Fc^2)/3$

[2] $R = \Sigma||F_o|-|F_c|| / \Sigma|F_o|$, $wR = \{\Sigma[w(|F_o|^2 - |F_c|^2)^2] /\Sigma[w(|F_o|^4)]\}^{1/2}$ and $w = 1/(\sigma^2(I) + 0.0004I^2)$

[3] $R = \Sigma||F_o|-|F_c|| / \Sigma|F_o|$, $wR = \{\Sigma[w(|F_o|^2 - |F_c|^2)^2] / \Sigma[w(|F_o|^4)]\}^{1/2}$ and $w=1/[\sigma^2(Fo^2)+(0.0001P)^2+373.8861P]$ where $P=(Fo^2+2Fc^2)/3$

[4] $R = \Sigma||F_o|-|F_c|| / \Sigma|F_o|$, $wR = \{\Sigma[w(|F_o|^2 - |F_c|^2)^2] / \Sigma[w(|F_o|^4)]\}^{1/2}$ and $w=1/[\sigma^2(Fo^2)+231.5294P]$ where $P=(Fo^2+2Fc^2)/3$

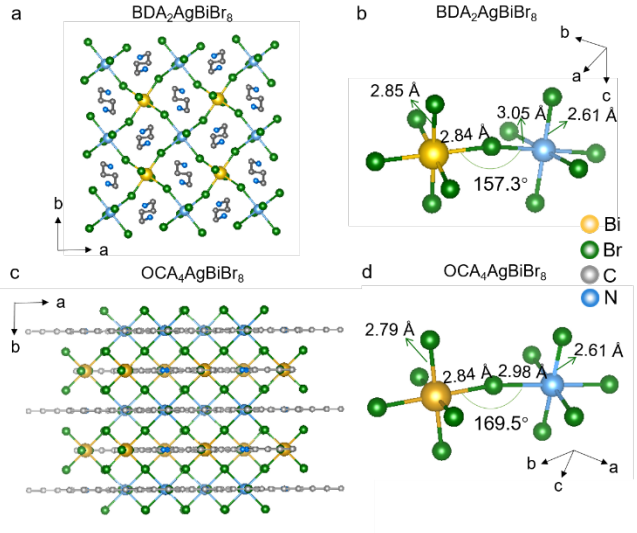

Figure 5. Crystal structures of $BDA_2AgBiBr_8$ and $OCA_4AgBiBr_8$. (a) and (c) show the top down view of the layer orientation. (b) and (d) are the local coordination environments for Ag and Bi for $BDA_2AgBiBr_8$ and $OCA_4AgBiBr_8$, respectively. Hydrogens are omitted for clarity.

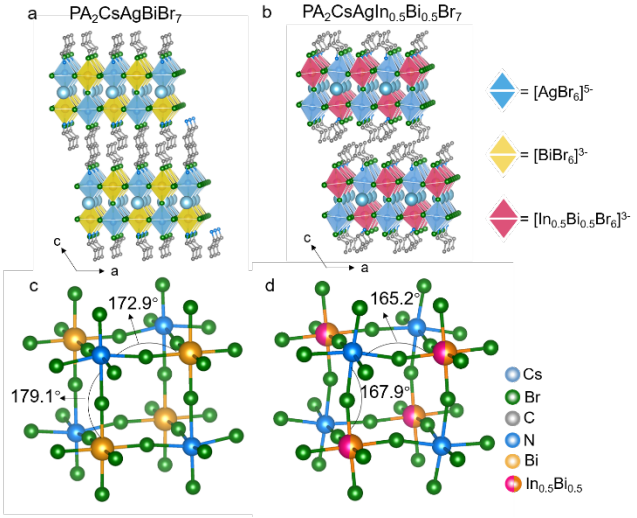

Figure 6. Crystal structures of the two-layered compounds (a) $PA_2CsAgBiBr_7$ and (b) $PA_2CsAgIn_{0.5}Bi_{0.5}Br_7$. (c) and (d) show the inorganic framework of the basic building unit and the M-Br-M angles of $PA_2CsAgBiBr_7$ and $PA_2CsAgIn_{0.5}Bi_{0.5}Br_7$. Hydrogens are omitted for clarity.

Changing M^{III} from In to Bi, $PA_4AgBiBr_8$ crystallizes in the monoclinic space group *C2/m*, which is expected to be the same as the previously reported structure $BA_4AgBiBr_8$ (BA = butylammonium).[36] Similar to the $PA_4AgInCl_8$ case, the Ag^I and Bi^{III} sites are clearly identifiable, and the Ag^I site still under goes distortion because of the compression of the axial Ag-Br bonds (2.65 Å vs. 3.00 Å). The Bi^{III} site remains rather undistorted, as all the Bi-Br bond lengths are ~2.82 Å and the Br-Bi-Br angles are ~90° (Figure 4f). Only one kind of hydrogen bond is observed in the structure, which is between N and the terminal Br on Bi. The donor-acceptor distance is 3.15 Å (Figure 4i). This particularly short H-bond could be explained by the more electron-positive nature of Bi (than In), which leads to a stronger interaction between the Br on Bi and H rather than the Br on In.

The single-layered hybrid double perovskites can be expanded by changing the organic cations. Short and long, singly and doubly protonated cations such as di-butylammonium (BDA) and octylammonium (OCA) have been successfully demonstrated in the Ag-Bi-Br system, where the interlayer distance varies from 9.49 Å to 20.72 Å shown in Figure 1d, e. $BDA_2AgBiBr_8$ belongs to the Dion-Jacobson (DJ) type[33,43] layered perovskites, where one spacing cation instead of two is in the interlayer space (Figure 2d). A distinct difference between the DJ and RP phases comes from the layer orientation, where in the DJ phase the layers lie on top of each other (Figure 5a) and in the RP phase the layers are shifted by (1/2, 0) (Figure 5c). The local octahedral environments of Ag^I and Bi^{III} are rather similar to $PA_4AgBiBr_8$, as seen in Figure 5b and 5d. One major difference in the layered double perovskite system compared with the Pb or Sn based layered perovskite system is that the metal-halide-metal (*M-X-M*) angles are not much involved in affecting the optical properties.[33,44] However, substantial change in the M^I-*X*-M^{III} is identified, where the smallest Ag-Br-Bi angle, 157.3˚, is seen in the BDA case. The angle increases to 163.8˚ in the PA structure, and increases further to 169.5˚ for the longest ammonium here OCA (Figure 5b, d). The much smaller interlayer distance in the DJ phase (9.49 Å) compared to the RP phase utilizing a long chain ammonium cation (20.72 Å) could potentially facilitate charge transfer between the inorganic layers like in the Pb-based systems.[31,33]

The double-layered structures, $PA_2CsAgBiBr_7$ and $PA_2CsAgIn_{0.5}Bi_{0.5}Br_7$ both crystallize in the monoclinic space group $P2_1/m$, as does the BA analogue.[36] The crystallographic refinement details are given in Table 2. The Cs^+ cations occupy the empty cavities in the inorganic cages, while the organic cations lie between the double layers. Alloying In and Bi in 1:1 ratio is accomplished, with a refined occupancy of In (0.48) and Bi (0.52). We have synthesized small amount of $PA_2CsAgInBr_7$, however, the poor quality of the crystals prohibits us to perform structural determination and further characterizations. Noticeable changes in the inorganic framework are shown in Figure 5c and d, where the Bi-Br-Bi angles decrease from 172.9˚ and 179.1˚ to 165.2˚ and 167.9˚, which is reasonable when alloying a much smaller metal cation (In) into the system. The alloying also causes shrinkage in the unit cell, the most pronounced change seen in c (from 18.536 (8) Å to 18.310 (2) Å).

Optical properties. In accordance with the parent 3D structure $Cs_2AgBiBr_6$, which has an indirect band gap, the 2D derivatives have similar absorption features, with slightly higher energy edge onsets corresponding to their lighter colors (Figure 2a-e). The absorption spectra of $PA_4AgBiBr_8$, $PA_2CsAgBiBr_7$, the butylammonium (BA) analogues and the 3D double perovskite $Cs_2AgBiBr_6$, are shown in Figure 6a for comparison. The single- and double-layered members of PA and BA have similar band gaps of 2.41 eV and 2.32 eV, respectively (Figure 6a). The band gap of $Cs_2AgBiBr_6$ measured by diffuse reflectance is 2.20 eV, similar to the previously reported value (2.19 eV).[17] For the rest of the single-layered members with different organic spacers, $BDA_2AgBiBr_8$ and $OCA_4AgBiBr_8$ have similar band gaps of 2.43 eV and 2.45 eV compared to $PA_4AgBiBr_8$ (2.41 eV) (Figure 7c), indicating that the effect of the organic spacers upon the magnitude of the optical gap is minimal. In Pb- or Sn-based layered systems, the organic cations effectively affect the band gap by impacting the respective *M-X-M* angles.[33,44] For $PA_4AgInBr_8$, a sharp absorption edge of 3.15 eV is estimated as

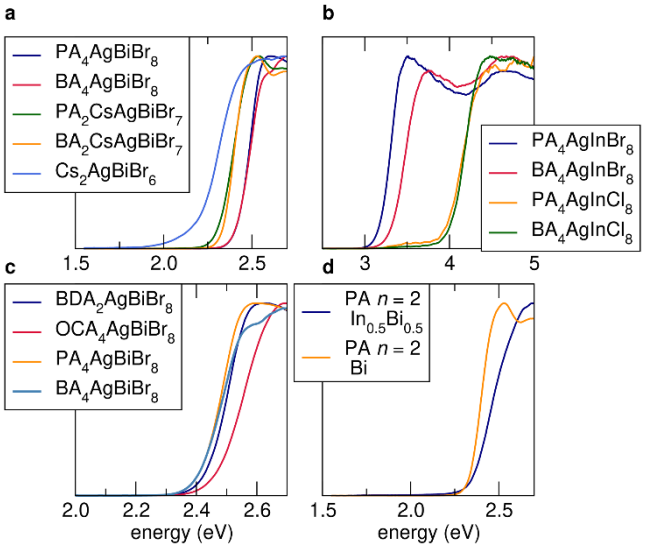

Figure 7. Optical absorption spectra of (a) $PA_4AgBiBr_8$, $PA_2CsAgBiBr_7$ with the BA analogues and the 3D double perovskite $Cs_2AgBiBr_6$. (b) $PA_4AgInBr_8$, $PA_4AgInCl_8$ and their BA analogues for comparison. (c) Changing the organic spacers in the Ag-Bi-Br single-layered system. (d) $PA_2CsAgBiBr_7$ and $PA_2CsAgIn_{0.5}Bi_{0.5}Br_7$.

the band gap of this material. The BA analogue has an absorption edge at higher energy of 3.32 eV (Figure 7b). The direct band gap 3D double perovskite $Cs_2AgInCl_6$ has a reported band gap of 3.23 eV.[22] The 2D derivative compounds $PA_4AgInCl_8$ and $BA_4AgInCl_8$ have a larger band gaps of 3.96 eV. In contrast to the Pb- and Sn- based 2D systems, excitonic absorption features associated with the 2D confinement are not clearly observed in the layered double perovskites measured by diffuse reflectance spectra. This observation is similar to the previously reported layered double perovskites, where the low energy absorptions are relatively broad compared to the Pb-based systems.[39] Alloying Bi and In in $PA_2CsAgBiBr_7$ increases the band gap slightly as seen in Figure 7d, from 2.32 eV to 2.35 eV.

Table 3. Summary of band gaps and PL emission energies of selected compounds.

Compound	E_g (eV)	PL (eV)
$PA_4AgBiBr_8$	2.41	*NA*
$PA_4AgSb_{0.5}Bi_{0.5}Br_8$	2.51	1.93
$PA_4AgIn_{0.5}Bi_{0.5}Br_8$	2.56	1.76
$PA_4AgInBr_8$	3.15	2.76
$PA_4AgInCl_8$	3.96	*NA*
*$Cs_2AgBiBr_6$	2.20	1.91

Weak photoluminescence (PL) is observed in the 2D layered double perovskite system (Figure 8), with most of the PL are only observable at low temperatures. The PL for pristine $PA_4AgBiBr_8$ is too weak, which needs further validation under more extreme experimental conditions (e.g. lower temperature or under-pressure). The PL emission peaks of $PA_4AgInBr_8$, $PA_4AgSb_{0.5}Bi_{0.5}Br_8$ and $PA_4AgIn_{0.5}Bi_{0.5}Br_8$ emit across the range of 449-705 nm at 100 K, exhibiting a wide range of tunability. Detailed PL emission energies and the corresponding band gap are given in Table 3. Temperature-dependent PL data were collected for $PA_4AgSb_{0.5}Bi_{0.5}Br_8$ (as it emits brighter) and the PL gradually quenches with increasing temperature to room temperature (Figure 8b). The PL emission center and bandwidth remain unchanged. The generally broad PL, especially with the Bi/Sb and Bi/In solid solutions, are similar to what were observed in the $A_3M_2I_9$ systems (A = Rb, Cs; M = Sb, Bi). This could be due to self-trapped excitons (STEs) arising from electron-phonon coupling.[45,46] The large Stokes shifts of $PA_4AgSb_{0.5}Bi_{0.5}Br_8$ and $PA_4AgIn_{0.5}Bi_{0.5}Br_8$ are possibly originated from STEs, as previously seen in $(tms)_4Pb_3Br_{10}$ (tms =

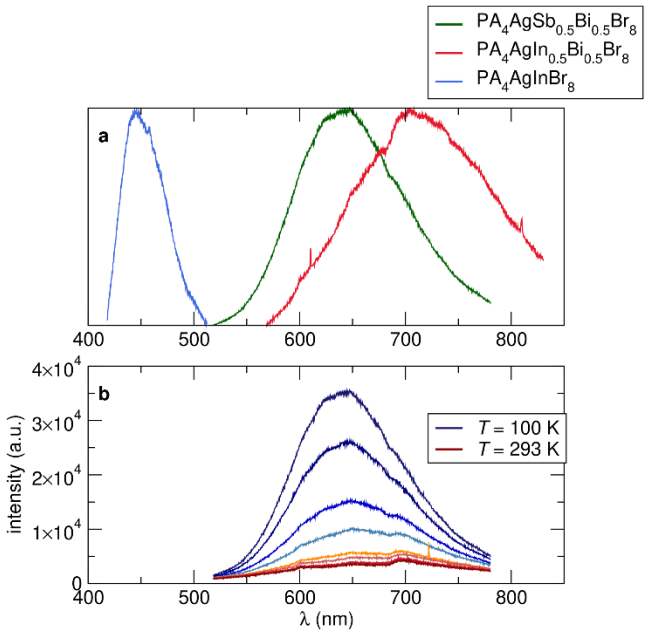

Figure 8. Steady-state photoluminescence (PL) spectra at 100K for (a) $PA_4AgInBr_8$, $PA_4AgSb_{0.5}Bi_{0.5}Br_8$ and $PA_4AgIn_{0.5}Bi_{0.5}Br_8$. (b) Temperature-dependent PL for $PA_4AgSb_{0.5}In_{0.5}Br_8$ from 100 K to 293K.

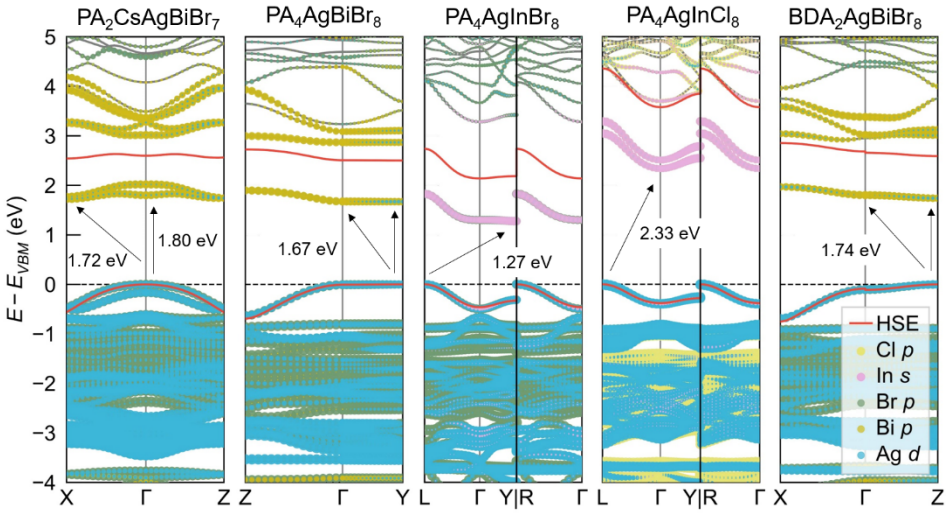

Figure 9. DFT PBE band structure calculations for $PA_2CsAgBiBr_7$, $PA_4AgBiBr_8$, $PA_4AgInBr_8$, $PA_4AgInCl_8$ and $BDA_2AgBiBr_8$ from left to right. Orbital projections are represented as circles with sizes corresponding to relative contributions. The conduction and valence bands calculated using the HSE06 functional are additionally overlaid.

trimethylsulfonium), which has a layered structure with large Stokes shift and broad PL emission. [47]

Band structure calculations. To complement our experimental results, we performed first-principles simulations in order to understand the influence of these new structures and compositions on the electronic transitions. The band structures in Figure 9 summarize our major findings. Overall, these calculations qualitatively match our experimental findings: the band gap of the single-layered compound $PA_4AgBiBr_8$ is smaller than the corresponding two-layered compound, $PA_2CsAgBiBr_7$, and the band gap of the chloride, $PA_4AgInCl_8$, exceeds that of the corresponding bromide, $PA_4AgInBr_8$. We performed calculations with and without the inclusion of spin-orbit coupling (SOC) effects and found, that SOC has a significant impact on the band gap in compounds containing Bi^{3+}, which have significant Bi *p* character in the conduction band. SOC has little effect on the band gap of compounds containing the In^{III} ion, which have predominant In *s* character in the conduction band. In addition to the greater mass of Bi, which increases the magnitude of the SOC, the lack of orbital angular momentum in the In *s* (l=0) state greatly reduces the impact of SOC on the conduction band in the In compounds. A good understanding of the conduction band character and the influence of spin-orbit coupling can therefore be gained by simply considering the orbital filling of the M^{III} cations. The predominant character of the bands below the band gap results from a combination of Ag *d* and *X p* states. Right at the VBM in the Bi^{3+} compounds, there is a small lone-pair contribution from Bi *s* orbitals as in other similar halide perovskite-related materials. Bi *s* and Ag *s* contributions are plotted in Figure S6.

With the aim of obtaining better quantitative matching with our experimental results, we also compared our results with calculations using the HSE06 functional, which is known to improve band gap estimation across a wide population of semiconductors.[48] The HSE06 band gaps are much closer to the experimentally determined values for all our materials. However, there is a significant discrepancy between the calculated and measured band gap of $PA_4AgInBr_8$ even with HSE06 (Table S4).

Connor and coworkers considered the related systems, $BA_2CsAgBiBr_7$ and $BA_4AgBiBr_8$, concluding based on first-principles calculations on those systems, as well as related, layered systems, that there should be an indirect to direct band gap transition with reduction in the layer parameter, n.[36] We find that none of our RP prototype structures have true direct band gaps, although $BA_4AgBiBr_8$ has valley degeneracy resulting in equal indirect and direct gaps. Given the chemical similarity between the DJ phase $BDA_2AgBiBr_8$—which has a low-dispersion conduction band with the smallest direct band gap transition—and the other structures considered, the structure archetype (DJ/RP) may be even more important than the layering for the direct / indirect transition in this system.

As a final note, we want to caution against strong statements about the location of the conduction band maxima and minima of the calculated band gaps in materials with exceptionally flat conduction bands such as $PA_2CsAgBiBr_7$, $PA_4AgBiBr_8$, and $BDA_2AgBiBr_8$. Due to computational expense, simulations are frequently performed on idealized structures in which organic cations are replaced with ions such as Cs^+, or by using only a single functional. For these flat band compounds, we find that both explicit inclusion of the organic spacer and the choice of functional can change the location of the conduction band minimum within the Brillouin zone, although the *dispersion* for the bands is largely qualitatively unchanged. Brillouin zone locations and values of all calculated band gaps are available in Tables S1-3.

CONCLUSIONS

In conclusion, we have designed and synthesized seven new hybrid layered cation-ordered perovskite halides with different structures and compositions. Unlike conventional Pb-based 2D systems, the excitonic features are less visible, and so far, appear to possess limited ability to be built into higher (than n = 2) layer numbers using solution methods. These compounds are promising in the sense that (i) a wide range of organic spacing cations can be used (here PA, BA, BDA and OCA); (ii) tunable layer thickness can be achieved, (iii) a metal alloying strategy on both 1+ and 3+ sites can be carried out; and (iv) varying the

halide can be used to control the optoelectronic properties. We have showcased some of our successful syntheses with detailed structural analysis of these new materials, and optical characterization. The realization of these new structures further enlarges the scope of layered double perovskite halides, and points to the possibility of synthesizing a huge range of accessible materials with interesting and tunable optoelectronic properties.

METHODS

Materials. $InCl_3$ (98%), Sb_2O_3 (99%), silver acetate (99%), propylamine (98%), butylamine (99.5%), 1,4-diaminobutane (99%), octylamine (99%), hydrochloric acid (semiconductor grade, 37%), hydrobromic acid (ACS reagent, 48%) were purchased from Sigma-Aldrich and used as received. Bi_2O_3 (99.9%), CsBr (99%) were purchased from Alfa Aesar and used as received.

Synthesis of $PA_4AgInCl_8$. 333.8 mg (2 mmol) of silver acetate and 442.4 mg (2 mmol) of $InCl_3$ were dissolved in 6 mL of HCl. 1 ml of propylamine was added to the previous solution before heating and stirring at 108 °C. After heating and stirring for 5-10 min, white precipitates formed. Clear solution was obtained after filtering out the white precipitates, and continued to be heated and stirred for another 10 min at 108 °C. Colorless plate-like crystals precipitated during slow-cooling to room temperature. Yield 125 mg (8.4% based on total In content). The low yield of $PA_4AgInCl_8$ is primarily due to several filtrations during the synthesis to exclude AgCl precipitate, which filter most of the starting materials out. An analogous procedure was used to synthesize $BA_4AgInCl_8$ for comparison of the band gap.

Synthesis of $PA_4AgInBr_8$. 166.9 mg (1 mmol) of silver acetate and 221.2 mg (1 mmol) of $InCl_3$ were dissolved in 5 mL of HBr. 0.5 ml of propylamine was added to the previous solution before heating and stirring at 122 °C for 10 min until the solution turned clear. Colorless plate-like crystals precipitated during slow-cooling to room temperature. Minor yellow impurities were observed forming on the surface of the solution. Yield 415 mg (37.7% based on total In content). An analogous procedure was used to synthesize $BA_4AgInBr_8$ for comparison of the band gap.

Synthesis of $PA_4AgBiBr_8$. 166.9 mg (1 mmol) of silver acetate and 466 mg (1 mmol) of Bi_2O_3 were dissolved in 5 mL of HBr. 0.5 ml of propylamine was added to the previous solution before heating and stirring at 122 °C for 10 min until the solution turned clear. Yellow plate-like crystals precipitated during slow-cooling to room temperature. Yield 365 mg (30.5% based on total Bi content). Analogous procedures were used to synthesize $BA_4AgBiBr_8$, $BDA_2AgBiBr_8$, $OCA_4AgBiBr_8$, $PA_4AgIn_{0.5}Bi_{0.5}Br_8$ (change to 0.5 mmol Bi_2O_3 and 0.5 mmol $InCl_3$) and $PA_4AgSb_{0.5}Bi_{0.5}Br_8$ (change to 0.5 mmol Bi_2O_3 and 0.5 mmol Sb_2O_3) for comparison of the band gaps.

Synthesis of $PA_2CsAgBiBr_7$ and $PA_2CsAgIn_{0.5}Bi_{0.5}Br_7$. 166.9 mg (1 mmol) of silver acetate, 212.8 mg (1 mmol) of CsBr and 466 mg (1 mmol) of Bi_2O_3 were dissolved in 8 mL of HBr. 160 mg of propylamine was added to the previous solution before heating and stirring at 122 °C for 10 min until the solution turned clear. Orange crystals ($Cs_2AgBiBr_6$, 3D phase) precipitated during slow-cooling to room temperature. Clear solution was obtained after filtering out the undesired orange 3D phase, and another 160 mg of propylamine was added before heating and stirring at 122 °C until solution turned clear. The same process was repeated again, ultimately no more orange phase was formed and yellow plate-like crystals precipitated during slow-cooling to room temperature. Yield 365 mg (30.5% based on total Bi content). $PA_2CsAgIn_{0.5}Bi_{0.5}Br_7$ was synthesized by dissolving 166.9 mg (1 mmol) of silver acetate, 212.8 mg (1 mmol) of CsBr, 233 mg (0.5 mmol) of Bi_2O_3 and 110.6 mg of $InCl_3$ (0.5 mmol) in 6 mL of HBr. 160 mg of propylamine was added to the above solution and stirring at 122 °C for 10 min until the solution turned clear. Orange phase of $Cs_2AgBiBr_6$ and unknown light-yellow phase precipitated during slow-cooling to room temperature. By filtering the above solution, the mother solution was kept undisturbed for 1-2 days and yellow plate-like crystals formed. Only small amount of $PA_2CsAgIn_{0.5}Bi_{0.5}Br_7$ was obtained, enough for single-crystal diffraction and optical absorption measurement.

Single Crystal X-ray Diffraction. Full sphere data were collected using a Bruker KAPPA APEX II diffractometer equipped with an APEX II CCD detector using a TRIUMPH monochromator with Mo Kα source (λ = 0.71073 Å) with MX Optics or a Bruker D8 VENTURE diffractometer equipped with a Kappa goniometer stage a PHOTON II CPAD detector and an IμS 3.0 Mo Kα source (λ = 0.71073 Å). Data were collected at 293K. The collected data were integrated and applied with multi-scan absorption correction using the APEX2 or APEX3 software. Crystal structures were solved by direct methods (Full-matrix least-squares on F^2) and refined by full-matrix least-squares on F^2 using the OLEX2 program package[49] and by charge flipping (full-matrix least-squares on F^2) using the Jana2006 package.

Transmission Electron Microscopy (TEM). Transmission Electron Microscopy (TEM) and Selected Area Electron Diffraction (SAED) images were acquired using an FEI Tecnai G2 Sphera operating at 200 keV in bright field mode. n = 1 PAI crystals were crushed onto TEM grids (Ted Pella No. 01824, ultrathin C film on holey carbon support film, 400 mesh, Cu) using a razor blade. Prior to crushing, the n = 1 PAI crystals were rinsed with ether to remove residual HI. With intention to reduce beam damage and obtain diffraction patterns of the smallest area possible, a spot size of (5) was selected for both real-space and SAED imaging. The scale for both the SAED and real-space images was calibrated using Au nanoparticle. An objective aperture was not employed for imaging.

Optical Absorption Spectroscopy. Optical diffuse reflectance measurements were performed using a Shimadzu UV-3600 UV-VIS-NIR spectrometer operating in the 220–1000 nm region using $BaSO_4$ as the reference of 100% reflectance. The band gap of the material was estimated by converting reflectance to absorption according to the Kubelka–Munk equation: $\alpha/S = (1-R)^2(2R)^{-1}$, where R is the reflectance and α and S are the absorption and scattering coefficients, respectively.

Steady-state Photoluminescence. Steady-state PL was measured from samples at 100 K. Crystals were extracted from solution, dried using filter paper, and piled with random orientations on 0.18mm glass substrates. Substrates were then placed directly on the heating/cooling block of a temperature-controlled stage ("cryostage") (Linkam HFS600E-P). Clear glass windows were used to seal the cryostage. The cryostage was then evacuated to approximately 0.1 Torr, placed above the objective of an inverted microscope (Nikon Eclipse Ti-U), and cooled to 100K by active liquid nitrogen vapor flow using the LNP95 Liquid Nitrogen Cooling system. Crystals were illuminated by focusing a 405 nm laser (spot size of approximately 10 μm) through a 10x objective with a nominal laser output of approximately 1 mW (corresponding to approximately 10W/cm^2 at the level of the sample). PL was collected by the same 10x objective and projected to the entrance slit of an imaging spectrometer (Princeton IsoPlane SCT320) with an attached cooled CCD camera (Princeton PIXIS 1024). The excitation wavelengths were filtered out using a conventional three-element 405 nm filter cube (Semrock). Integration times were on the order of 10 seconds. Considering the high incident optical powers required to get a decent PL

signal, we conclude that PL yields of all materials are remarkably low. No signs of light-induced material degradation were observed.

Computational details. *Ab initio* calculations using VASP were performed on $PA_2CsAgBiBr_7$, $PA_4AgBiBr_8$, $PA_4AgInBr_8$, $PA_4AgInCl_8$, and $BDA_2AgBiBr_8$ using the projector augmented wave method and results were compared using the PBE and HSE06 functionals with and without spin-orbit coupling.[50-53,54,48,55] For those structures with no partial occupancies on the organic spacer molecules, PBE calculations were performed both on the full, room-temperature, experimental structures and model 'inorganic' structures in which the spacers were removed and NH_4^+ ions replaced with Cs^+ ions on the nitrogen sites. Cesium-substituted inorganic structures are frequently used to simulate the electronic structure of complex hybrid perovskite-derivatives, and have previously been applied to related compounds.[36] Due to computational constraints, hybrid calculations were only performed on the inorganic structures. We utilized fully automatic *k*-mesh generation with the 'length' parameter *l* set to 10, 20, and 30.[56] All calculations were compared using these three k-mesh densities and band gaps were found to be converged better than 0.1 eV for all materials. Reported values correspond to 'inorganic' simulations using the highest k-mesh settings, as well as a plane-wave energy cutoff of 400 eV (highest-density k-meshes were 4x4x2, 4x4x2, 4x4x2, 4x4x1, and 4x4x3 for $(PA)_2CsAgBiBr_7$, $(PA)_4AgBiBr_8$, $(PA)_4AgInBr_8$,$(PA)_4AgInCl_8$, and $(BDA)_2AgBiBr_8$, respectively). PBE band structures were calculated in a standard non-self consistent run using the charge density from an initial static calculation (HSE06 calculations can only be conducted self-consistently). All calculation steps had energy convergence better than 10^{-5} eV. A comparison of band gaps and the HOMO and LUMO locations in *k*-space are available in the SI.

ASSOCIATED CONTENT

X-ray crystallographic data (cif.), Powder X-ray diffraction (PXRD), diffuse reflectance spectra, additional photoluminescence (PL) data, additional calculation data and X-ray Fluorescence (XRF) results (pdf.) are available in the supporting information free of charge on the ACS Publications website.

AUTHOR INFORMATION

Corresponding Author

* ramseshadri@ucsb.edu
* akc30@cam.ac.uk

ORCID
Lingling Mao: 0000-0003-3166-8559
Samuel M. L. Teicher: 0000-0002-5922-4258
Constantinos C. Stoumpos: 0000-0001-8396-9578
Rhys M. Kennard: 0000-0003-1181-5638
Ryan A. DeCrescent: 0000-0003-3219-7736
Jon A. Schuller: 0000-0001-6949-3569
Michael L. Chabinyc: 0000-0003-4641-3508
Anthony K. Cheetham: 0000-0003-1518-4845
Ram Seshadri: 0000-0001-5858-4027

Notes

The authors declare no competing financial interest.

ACKNOWLEDGMENT

This work was supported by the Department of Energy, Office of Science, Basic Energy Sciences, under Grant SC0012541. The research reported here made use of the shared facilities of the Materials Research Science and Engineering Center at UC Santa Barbara, NSF DMR 1720256. The UCSB MRSEC is a member of the Materials Research Facilities Network (www.mrfn.org). R.M.K. gratefully acknowledges the National Defense Science and Engineering Graduate fellowship for financial support. This work is supported in part by the project "NANO-TANDEM" (MIS5029191), co-financed by Greece and the European Regional Development Fund.

REFERENCES

(1) Kojima, A.; Teshima, K.; Shirai, Y.; Miyasaka, T. Organometal Halide Perovskites as Visible-Light Sensitizers for Photovoltaic Cells. *J. Am. Chem. Soc.* **2009**, *131*, 6050-6051.

(2) Jena, A. K.; Kulkarni, A.; Miyasaka, T. Halide Perovskite Photovoltaics: Background, Status, and Future Prospects. *Chem. Rev.* **2019**, *119*, 3036-3103.

(3) Kovalenko, M. V.; Protesescu, L.; Bodnarchuk, M. I. Properties and potential optoelectronic applications of lead halide perovskite nanocrystals. *Science* **2017**, *358*, 745-750.

(4) Mao, L.; Stoumpos, C. C.; Kanatzidis, M. G. Two-Dimensional Hybrid Halide Perovskites: Principles and Promises. *J. Am. Chem. Soc.* **2019**, *141*, 1171-1190.

(5) Green, M. A.; Ho-Baillie, A.; Snaith, H. J. The emergence of perovskite solar cells. *Nat. Photonics* **2014**, *8*, 506.

(6) Zhou, H.; Chen, Q.; Li, G.; Luo, S.; Song, T.-b.; Duan H.-S.; Hong, Z.; You, J.; Liu, Y.; Yang, Y. Interface engineering of highly efficient perovskite solar cells. *Science* **2014**, *345*, 542-546.

(7) Bai, S.; Da, P.; Li, C.; Wang, Z.; Yuan, Z.; Fu, F.; Kawecki, M.; Liu, X.; Sakai, N.; Wang, J. T.-W.; Huettner, S.; Buecheler, S.; Fahlman, M.; Gao, F.; Snaith, H. J. Planar perovskite solar cells with long-term stability using ionic liquid additives. *Nature* **2019**, *571*, 245-250.

(8) Zhao, B.; Bai, S.; Kim, V.; Lamboll, R.; Shivanna, R.; Auras, F.; Richter, J. M.; Yang, L.; Dai, L.; Alsari, M.; She, X.-J.; Liang, L.; Zhang, J.; Lilliu, S.; Gao, P.; Snaith, H. J.; Wang, J.; Greenham, N. C.; Friend, R. H.; Di, D. High-efficiency perovskite–polymer bulk heterostructure light-emitting diodes. *Nat. Photonics* **2018**, *12*, 783-789.

(9) Zhang, Q.; Tavakoli, M. M.; Gu, L.; Zhang, D.; Tang, L.; Gao, Y.; Guo, J.; Lin, Y.; Leung, S.-F.; Poddar, S.; Fu, Y.; Fan, Z. Efficient metal halide perovskite light-emitting diodes with significantly improved light extraction on nanophotonic substrates. *Nat. Commun.* **2019**, *10*, 727.

(10) Xu, W.; Hu, Q.; Bai, S.; Bao, C.; Miao, Y.; Yuan, Z.; Borzda, T.; Barker, A. J.; Tyukalova, E.; Hu, Z.; Kawecki, M.; Wang, H.; Yan, Z.; Liu, X.; Shi, X.; Uvdal, K.; Fahlman, M.; Zhang, W.; Duchamp, M.; Liu, J.-M.; Petrozza, A.; Wang, J.; Liu, L.-M.; Huang, W.; Gao, F. Rational molecular passivation for high-performance perovskite light-emitting diodes. *Nat. Photonics* **2019**, *13*, 418-424.

(11) Shen, Y.; Cheng, L.-P.; Li, Y.-Q.; Li, W.; Chen, J.-D.; Lee, S.-T.; Tang, J.-X. High-Efficiency Perovskite Light-Emitting Diodes with Synergetic Outcoupling Enhancement. *Adv. Mater.* **2019**, *31*, 1901517.

(12) Stoumpos, C. C.; Kanatzidis, M. G. The Renaissance of Halide Perovskites and Their Evolution as Emerging Semiconductors. *Acc. Chem. Res.* **2015**, *48*, 2791-2802.

(13) Meyer, E.; Mutukwa, D.; Zingwe, N.; Taziwa, R. Lead-Free Halide Double Perovskites: A Review of the Structural, Optical, and Stability Properties as Well as Their Viability to Replace Lead Halide Perovskites. *Metals* **2018**, *8*, 667.

(14) Deng, W.; Deng, Z.-Y.; He, J.; Wang, M.; Chen, Z.-X.; Wei, S.-H.; Feng, H.-J. Synthesis of $Cs_2AgSbCl_6$ and improved optoelectronic properties of $Cs_2AgSbCl_6/TiO_2$ heterostructure

driven by the interface effect for lead-free double perovskites solar cells. *Appl. Phys. Lett.* **2017**, *111*, 151602.
(15) Wei, F.; Deng, Z.; Sun, S.; Hartono, N. T. P.; Seng, H. L.; Buonassisi, T.; Bristowe, P. D.; Cheetham, A. K. Enhanced visible light absorption for lead-free double perovskite $Cs_2AgSbBr_6$. *Chem. Comm.* **2019**, *55*, 3721-3724.
(16) Tran, T. T.; Panella, J. R.; Chamorro, J. R.; Morey, J. R.; McQueen, T. M. Designing indirect–direct bandgap transitions in double perovskites. *Mater. Horiz.* **2017**, *4*, 688-693.
(17) McClure, E. T.; Ball, M. R.; Windl, W.; Woodward, P. M. Cs_2AgBiX_6 (X = Br, Cl): New Visible Light Absorbing, Lead-Free Halide Perovskite Semiconductors. *Chem. Mater.* **2016**, *28*, 1348-1354.
(18) Majher, J. D.; Gray, M. B.; Strom, T. A.; Woodward, P. M. $Cs_2NaBiCl_6$: Mn^{2+}—A New Orange-Red Halide Double Perovskite Phosphor. *Chem. Mater.* **2019**, *31*, 1738-1744.
(19) Slavney, A. H.; Hu, T.; Lindenberg, A. M.; Karunadasa, H. I. A Bismuth-Halide Double Perovskite with Long Carrier Recombination Lifetime for Photovoltaic Applications. *J. Am. Chem. Soc.* **2016**, *138*, 2138-2141.
(20) Slavney, A. H.; Leppert, L.; Bartesaghi, D.; Gold-Parker, A.; Toney, M. F.; Savenije, T. J.; Neaton, J. B.; Karunadasa, H. I. Defect-Induced Band-Edge Reconstruction of a Bismuth-Halide Double Perovskite for Visible-Light Absorption. *J. Am. Chem. Soc.* **2017**, *139*, 5015-5018.
(21) Slavney, A. H.; Leppert, L.; Saldivar Valdes, A.; Bartesaghi, D.; Savenije, T. J.; Neaton, J. B.; Karunadasa, H. I. Small-Band-Gap Halide Double Perovskites. *Angew. Chem. Int. Ed.* **2018**, *57*, 12765-12770.
(22) Zhou, J.; Xia, Z.; Molokeev, M. S.; Zhang, X.; Peng, D.; Liu, Q. Composition design, optical gap and stability investigations of lead-free halide double perovskite $Cs_2AgInCl_6$. *J. Mater. Chem. A* **2017**, *5*, 15031-15037.
(23) Wei, F.; Deng, Z.; Sun, S.; Xie, F.; Kieslich, G.; Evans, D. M.; Carpenter, M. A.; Bristowe, P. D.; Cheetham, A. K. The synthesis, structure and electronic properties of a lead-free hybrid inorganic–organic double perovskite $(MA)_2KBiCl_6$ (MA = methylammonium). *Mater. Hor.* **2016**, *3*, 328-332.
(24) Deng, Z.; Wei, F.; Brivio, F.; Wu, Y.; Sun, S.; Bristowe, P. D.; Cheetham, A. K. Synthesis and Characterization of the Rare-Earth Hybrid Double Perovskites: $(CH_3NH_3)_2KGdCl_6$ and $(CH_3NH_3)_2KYCl_6$. *J. Phys. Chem. Lett.* **2017**, *8*, 5015-5020.
(25) Wei, F.; Deng, Z.; Sun, S.; Zhang, F.; Evans, D. M.; Kieslich, G.; Tominaka, S.; Carpenter, M. A.; Zhang, J.; Bristowe, P. D.; Cheetham, A. K. Synthesis and Properties of a Lead-Free Hybrid Double Perovskite: $(CH_3NH_3)_2AgBiBr_6$. *Chem. Mater.* **2017**, *29*, 1089-1094.
(26) Evans, H. A.; Schueller, E. C.; Smock, S. R.; Wu, G.; Seshadri, R.; Wudl, F. Perovskite-related hybrid noble metal iodides: Formamidinium platinum iodide [$(FA)_{(2)}(PtI_6)$-I-IV] and mixed-valence methylammonium gold iodide [$(MA)_{(2)}(AuAuI_6)$-Au-II-III]. *Inorganica Chim. Acta* **2018**, *482*, 469-469.
(27) Giustino, F.; Snaith, H. J. Toward Lead-Free Perovskite Solar Cells. *ACS Energy Lett.* **2016**, *1*, 1233-1240.
(28) Maughan, A. E.; Ganose, A. M.; Scanlon, D. O.; Neilson, J. R. Perspectives and Design Principles of Vacancy-Ordered Double Perovskite Halide Semiconductors. *Chem. Mater.* **2019**, *31*, 1184-1195.
(29) Evans, H. A.; Fabini, D. H.; Andrews, J. L.; Koerner, M.; Preefer, M. B.; Wu, G.; Wudl, F.; Cheetham, A. K.; Seshadri, R. Hydrogen Bonding Controls the Structural Evolution in Perovskite-Related Hybrid Platinum(IV) Iodides. *Inorg. Chem.* **2018**, *57*, 10375-10382.
(30) Lee, B.; Stoumpos, C. C.; Zhou, N.; Hao, F.; Malliakas, C.; Yeh, C.-Y.; Marks, T. J.; Kanatzidis, M. G.; Chang, R. P. H. Air-Stable Molecular Semiconducting Iodosalts for Solar Cell Applications: Cs_2SnI_6 as a Hole Conductor. *J. Am. Chem. Soc.* **2014**, *136*, 15379-15385.
(31) Stoumpos, C. C.; Cao, D. H.; Clark, D. J.; Young, J.; Rondinelli, J. M.; Jang, J. I.; Hupp, J. T.; Kanatzidis, M. G. Ruddlesden–Popper Hybrid Lead Iodide Perovskite 2D Homologous Semiconductors. *Chem. Mater.* **2016**, *28*, 2852-2867.
(32) Stoumpos, C. C.; Soe, C. M. M.; Tsai, H.; Nie, W.; Blancon, J.-C.; Cao, D. H.; Liu, F.; Traoré, B.; Katan, C.; Even, J. High members of the 2D Ruddlesden-Popper halide perovskites: synthesis, optical properties, and solar cells of $(CH_3(CH_2)_3NH_3)_2(CH_3NH_3)_4Pb_5I_{16}$. *Chem* **2017**, *2*, 427-440.
(33) Mao, L.; Ke, W.; Pedesseau, L.; Wu, Y.; Katan, C.; Even, J.; Wasielewski, M. R.; Stoumpos, C. C.; Kanatzidis, M. G. Hybrid Dion–Jacobson 2D Lead Iodide Perovskites. *J. Am. Chem. Soc.* **2018**, *140*, 3775-3783.
(34) Mao, L.; Kennard, R. M.; Traore, B.; Ke, W.; Katan, C.; Even, J.; Chabinyc, M. L.; Stoumpos, C. C.; Kanatzidis, M. G. Seven-Layered 2D Hybrid Lead Iodide Perovskites. *Chem* **2019**, *5*, 2593-2604.
(35) Tulsky, E. G.; Long, J. R. Dimensional Reduction: A Practical Formalism for Manipulating Solid Structures. *Chem. Mater.* **2001**, *13*, 1149-1166.
(36) Connor, B. A.; Leppert, L.; Smith, M. D.; Neaton, J. B.; Karunadasa, H. I. Layered Halide Double Perovskites: Dimensional Reduction of $Cs_2AgBiBr_6$. *J. Am. Chem. Soc.* **2018**, *140*, 5235-5240
.(37) Fang, Y.; Zhang, L.; Wu, L.; Yan, J.; Lin, Y.; Wang, K.; Mao, W. L.; Zou, B. Pressure-Induced Emission (PIE) and Phase Transition of a Two-dimensional Halide Double Perovskite $(BA)_4AgBiBr_8$ ($BA = CH_3(CH_2)_3NH_3^+$). *Angew. Chem. Int. Ed.*, *58*, 15249–15253.
(38) Sun, Z.; Xu, Z.; Liu, X.; Li, Y.; Liu, X.; Yang, T.; Ji, C.; Han, S.; Xu, Y.; Luo, J. Exploring Lead-free Hybrid Double Perovskite Crystals of $(BA)_2CsAgBiBr_7$ with Large Mobility-Lifetime Product toward X-ray Detection. *Angew. Chem. Int. Ed.*, *58*, 15757-15761.
(39) Jana, M. K.; Janke, S. M.; Dirkes, D. J.; Dovletgeldi, S.; Liu, C.; Qin, X.; Gundogdu, K.; You, W.; Blum, V.; Mitzi, D. B. Direct-Bandgap 2D Silver–Bismuth Iodide Double Perovskite: The Structure-Directing Influence of an Oligothiophene Spacer Cation. *J. Am. Chem. Soc.* **2019**, *141*, 7955-7964.
(40) Bi, L.-Y.; Hu, Y.-Q.; Li, M.-Q.; Hu, T.; Zhang, H.-L.; Yin, X.; Que, W.; Lassoued, M. S.; Zheng, Y.-Z. Two-dimensional lead-free iodide-based hybrid double perovskites: crystal growth, thin-film preparation and photocurrent responses. *J. Mater. Chem. A* **2019**, *7*, 19662-19667.
(41) Saparov, B.; Mitzi, D. B. Organic–inorganic perovskites: structural versatility for functional materials design. *Chem. Rev.* **2016**, *116*, 4558-4596.
(42) Steiner, T. The hydrogen bond in the solid state. *Angew. Chem. Int. Ed.* **2002**, *41*, 48-76.
(43) Dion, M.; Ganne, M.; Tournoux, M. Nouvelles familles de phases $M^{I}M^{II2}Nb_3O_{10}$ a feuillets "perovskites". *Mater. Res. Bull.* **1981**, *16*, 1429-1435.
(44) Knutson, J. L.; Martin, J. D.; Mitzi, D. B. Tuning the Band Gap in Hybrid Tin Iodide Perovskite Semiconductors Using Structural Templating. *Inorg. Chem.* **2005**, *44*, 4699-4705.
(45) McCall, K. M.; Stoumpos, C. C.; Kostina, S. S.; Kanatzidis, M. G.; Wessels, B. W. Strong Electron–Phonon Coupling and Self-Trapped Excitons in the Defect Halide Perovskites $A_3M_2I_9$ (A = Cs, Rb; M = Bi, Sb). *Chem. Mater.* **2017**, *29*, 4129-4145.
(46) McCall, K. M.; Stoumpos, C. C.; Kontsevoi, O. Y.; Alexander, G. C. B.; Wessels, B. W.; Kanatzidis, M. G. From 0D $Cs_3Bi_2I_9$ to 2D $Cs_3Bi_2I_6Cl_3$: Dimensional Expansion Induces a Direct Band Gap but Enhances Electron–Phonon Coupling. *Chem. Mater.* **2019**, *31*, 2644-2650.
(47) Smith, M. D.; Watson, B. L.; Dauskardt, R. H.; Karunadasa, H. I. Broadband Emission with a Massive Stokes Shift

from Sulfonium Pb–Br Hybrids. *Chemistry of Materials* **2017**, *29*, 7083-7087.
(48) Heyd, J.; Scuseria, G. E.; Ernzerhof, M. Hybrid functionals based on a screened Coulomb potential. *J. Chem. Phys.* **2003**, *118*, 8207-8215.
(49) Dolomanov, O. V.; Bourhis, L. J.; Gildea, R. J.; Howard, J. A.; Puschmann, H. OLEX2: a complete structure solution, refinement and analysis program. *J. Appl. Crystallogr.* **2009**, *42*, 339-341.
(50) Kresse, G.; Hafner, J. Ab initio molecular-dynamics simulation of the liquid-metal--amorphous-semiconductor transition in germanium. *Phys. Rev. B* **1994**, *49*, 14251-14269.
(51) Kresse, G.; Furthmüller, J. Efficient iterative schemes for ab initio total-energy calculations using a plane-wave basis set. *Phys. Rev. B* **1996**, *54*, 11169-11186.
(52) Kresse, G.; Furthmüller, J. Efficiency of ab-initio total energy calculations for metals and semiconductors using a plane-wave basis set. *Comput. Mater. Sci.* **1996**, *6*, 15-50.
(53) Kresse, G.; Joubert, D. From ultrasoft pseudopotentials to the projector augmented-wave method. *Phys. Rev. B* **1999**, *59*, 1758-1775.
(54) PAW potentials were chosen based on the guidelines at: cms.mpi.univie.ac.at/vasp/vasp/Recommended_PAW_potentials_DFT_calculations_using_vasp_5_2.html
(55) Perdew, J. P.; Burke, K.; Ernzerhof, M. Generalized gradient approximation made simple. *Phys. Rev. Lett.* **1996**, *77*, 3865.
(56) See definition of the length parameter at: cms.mpi.univie.ac.at/vasp/vasp/Automatic_k_mesh_generation.html

TOC Graphic

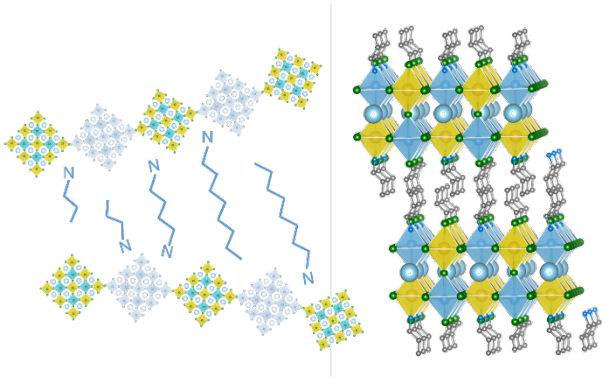

Supporting information for

Chemical and Structural Diversity of Hybrid Layered Double Perovskite Halides

Lingling Mao[1], Samuel M. L. Teicher [1], Constantinos C. Stoumpos[2], Rhys M. Kennard[1], Ryan A. DeCrescent[3], Guang Wu[4], Jon A. Schuller[5], Michael L. Chabinyc[1], Anthony K. Cheetham[1,6*] and Ram Seshadri[1,4*]

[1]Materials Research Laboratory and Materials Department, [3]Department of Physics, [4]Department of Chemistry and Biochemistry, [5]Department of Electrical and Computer Engineering, University of California, Santa Barbara, California 93106, United States

[2]Department of Materials Science and Technology, University of Crete, Vassilika Voutes GR-700 13 Heraklion, Greece

[6]Department of Materials Science & Engineering, National University of Singapore 9 Engineering Drive 1, Singapore 117576, Singapore

Table of contents

Table S1. Summary of new materials reported here.

Compound	Layer thickness (n)	Space group	Band gap (eV)
$PA_4AgInCl_8$	1	$P\bar{1}$	3.96
$BA_4AgInCl_8$	1	*NA*	3.99
$PA_4AgInBr_8$	1	$C2/m$	3.15
$BA_4AgInBr_8$	1	NA	3.30
$PA_4AgBiBr_8$	1	$C2/m$	2.41
$PA_4AgSb_{0.5}Bi_{0.5}Br_8$	1	*NA*	2.51
$PA_4AgIn_{0.5}Bi_{0.5}Br_8$	1	*NA*	2.56
$BDA_2AgBiBr_8$	1	$P\bar{1}$	2.43
$OCA_4AgBiBr_8$	1	$P2/m$	2.45
$PA_2CsAgBiBr_7$	2	$P2_1/m$	2.32
$PA_2CsAgIn_{0.5}Bi_{0.5}Br_7$	2	$P2_1/m$	2.35

Section S1. Powder X-ray Diffraction (PXRD)

PXRD analysis was performed using a Panalytical Empyrean powder diffractometer (Cu Kα source, λ = 1.5418 Å).

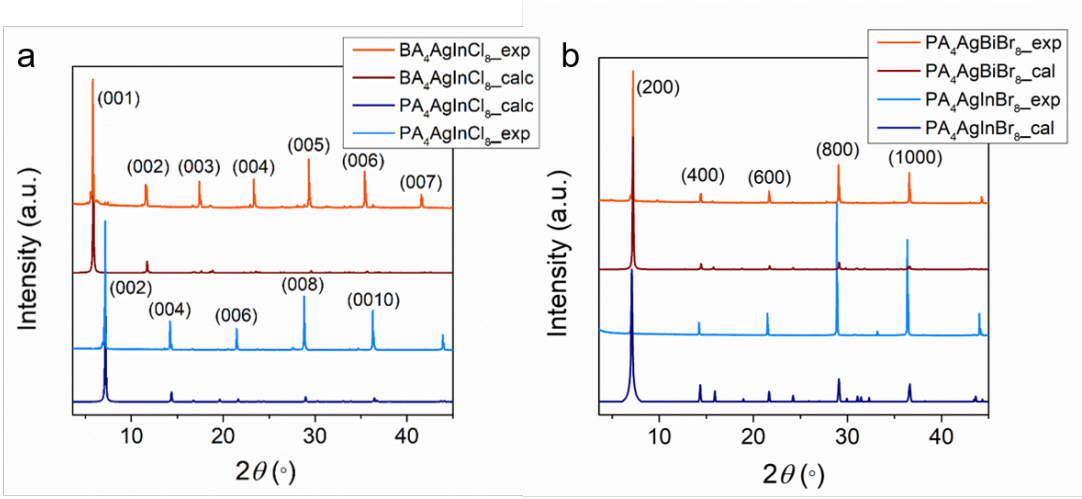

Figure S1. Experimental and calculated PXRD patterns of (a) $PA_4AgInCl_8$ and $BA_4AgInCl_8$ and (b) $PA_4AgInBr_8$ and $PA_4AgBiBr_8$. The peaks in the PXRD have strong preferred orientation along the (00*l*) or (*h*00) direction as labeled.

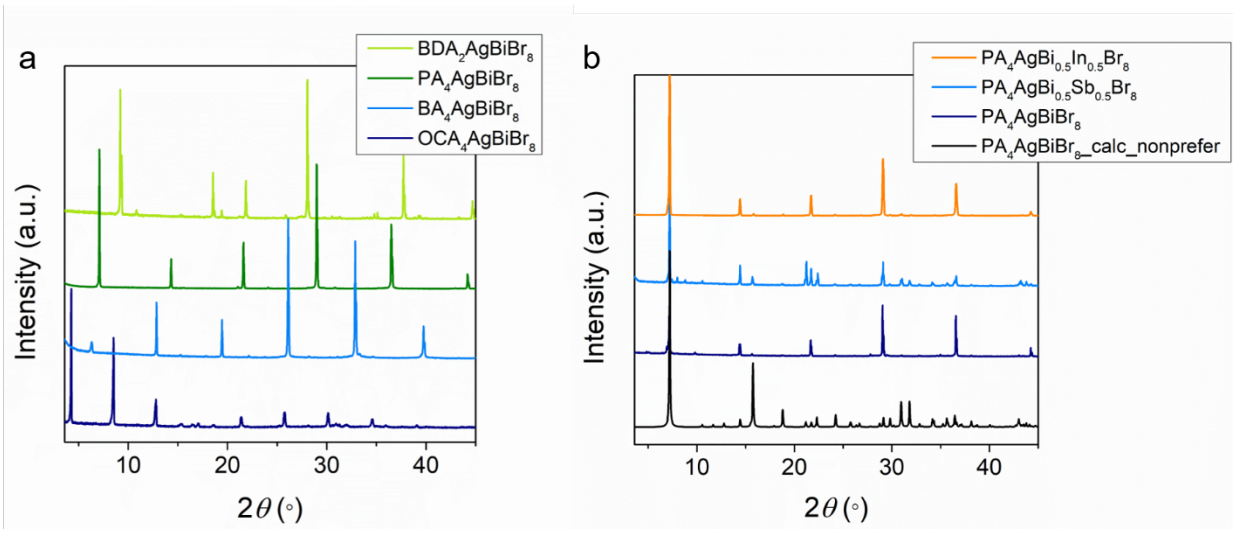

Figure S2. Experimental PXRD patterns of (a) $BDA_2AgBiBr_8$, $PA_4AgBiBr_8$, $BA_4AgBiBr_8$ and $OCA_4AgBiBr_8$. Shifting of the lowest angle peak in the spectra indicates the increasing in d-spacing. (b) $PA_4AgIn_{0.5}Bi_{0.5}Br_8$, $PA_4AgSb_{0.5}Bi_{0.5}Br_8$ and $PA_4AgBiBr_8$ (calculated and experimental for comparison).

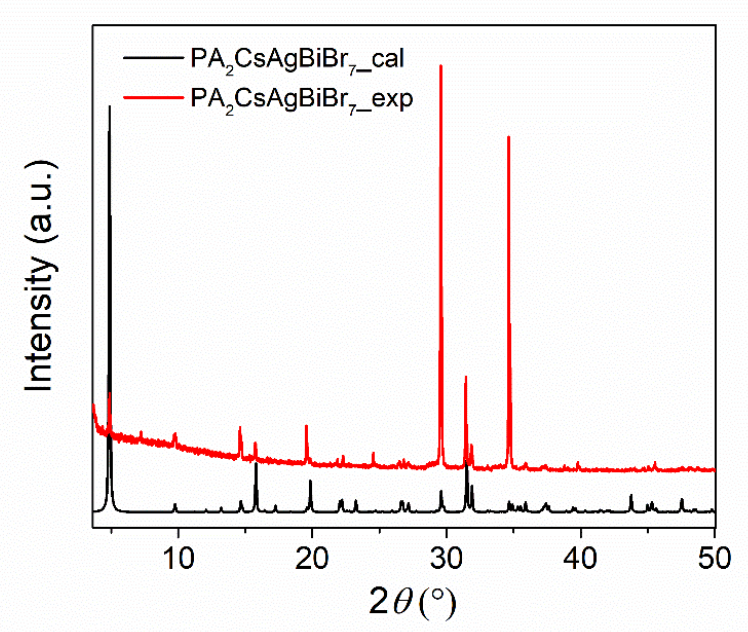

Figure S3. Experimental and calculated PXRD patterns of $PA_2CsAgBiBr_7$. The extra peak at ~7° belongs to the n = 1 impurity.

Section S2. Diffuse Reflectance Spectra

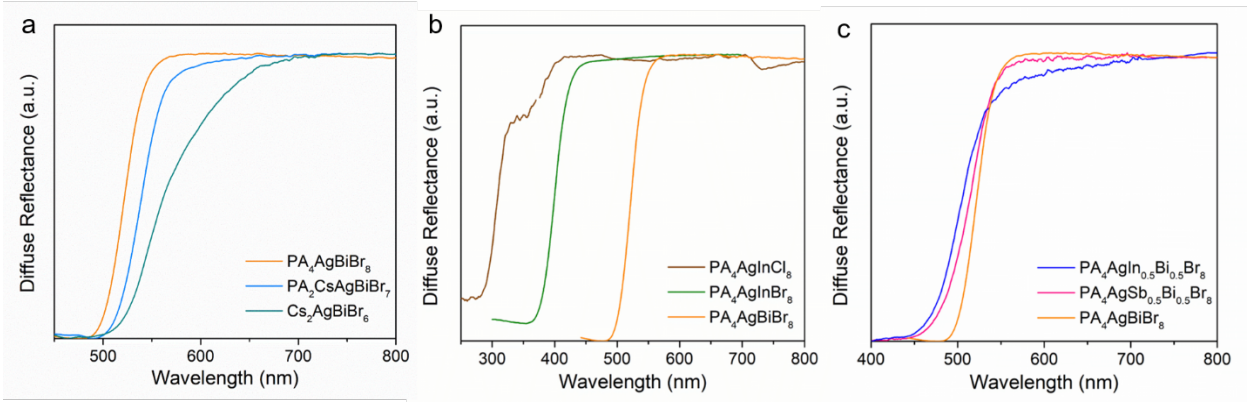

Figure S4. Diffuse reflectance spectra of (a) $PA_4AgBiBr_8$, $PA_2CsAgBiBr_7$ and $Cs_2AgBiBr_6$. (b) $PA_4AgInCl_8$, $PA_4AgInBr_8$ and $PA_4AgBiBr_8$. (c) $PA_4AgIn_{0.5}Bi_{0.5}Br_8$, $PA_4AgSb_{0.5}Bi_{0.5}Br_8$ and $PA_4AgBiBr_8$.

Section S3. Additional Photoluminescence (PL) data

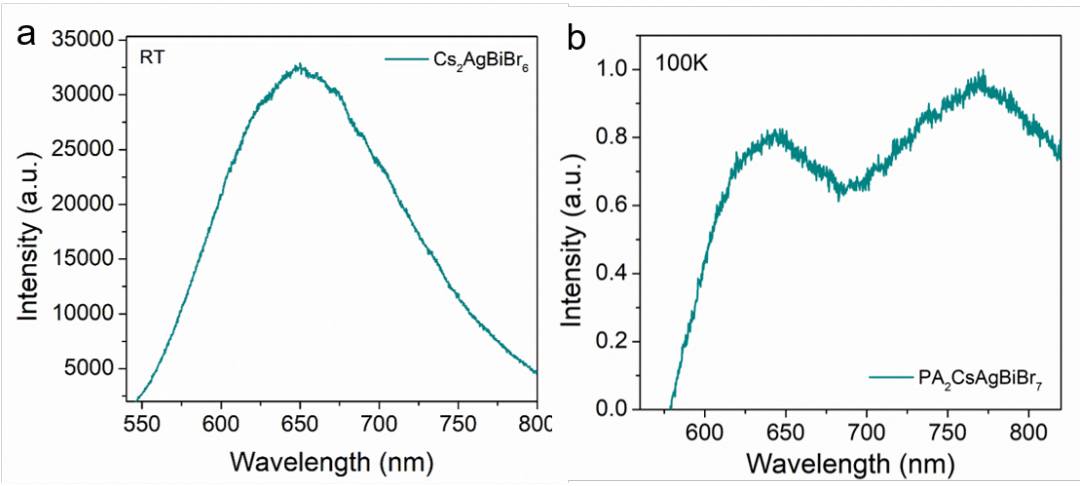

Figure S5. Steady-state photoluminescence (PL) spectra of (a) $Cs_2AgBiBr_6$ at room-temperature. (b) $PA_2CsAgBiBr_7$ at 100K.

Section S4. Additional Calculation data

Table S2. PBE band gaps (in eV), valence band minima and conduction band maxima for the cesium-substituted DFT cells discussed in the text. For indirect bandgaps, the smallest direct band gap is additionally listed.

Composition	w/o SOC				w/SOC			
	DBG	IBG	VBM	CBM	DBG	IBG	VBM	CBM
$PA_2CsAgBiBr_7$	2.303	1.954	*Γ*	*X*	1.801	1.724	*Γ*	*X*
$PA_4AgBiBr_8$	2.418	2.283	*Y*	*Z*	1.671	1.671	*Y*	*Y,Γ*
$PA_4AgInBr_8$	1.590	1.275	*L*	*Y*	1.585	1.274	*L*	*Y*
$PA_4AgInCl_8$	2.752	2.351	*L*	*Y*	2.731	2.336	*L*	*Y*
$BDA_2AgBiBr_8$	2.536	2.403	*Z*	*X*	1.740	N/A	*Z*	*Z*

Table S3. PBE band gaps (in eV), valence band minima and conduction band maxima for the full, unsubstituted unit cells of those compounds with no partial occupancies in the experimentally-solved structures. All values are close to those of the artificial, cesium-substituted cells described in the text, supporting the supposition that the organic spacers do not strongly influence the magnitude of the effective band gap.

Composition	w/o SOC				w/SOC			
	DBG	IBG	VBM	CBM	DBG	IBG	VBM	CBM
$PA_4AgInBr_8$	1.601	1.293	*L*	*Y*	1.594	1.291	*L*	*Y*
$PA_4AgInCl_8$	2.809	2.412	*R*	*Γ*	2.776	2.387	*L*	*Γ*
$BDA_2AgBiBr_8$	2.648	2.441	*Z*	*X*	1.794	N/A	*Z*	*Z*

Table S4. HSE band gaps (in eV), valence band minima and conduction band maxima for the cesium-substituted DFT cells discussed in the text.

Composition	w/SOC			
	DBG	IBG	VBM	CBM
$PA_2CsAgBiBr_7$	2.598	2.543	*Γ*	*X*
$PA_4AgBiBr_8$	2.503	2.503	*Y*	*Y,Γ*
$PA_4AgInBr_8$	2.515	2.138	*L*	*Γ*
$PA_4AgInCl_8$	3.955	3.574	*L*	*Γ*
$BDA_2AgBiBr_8$	2.591	N/A	*Z*	*Z*

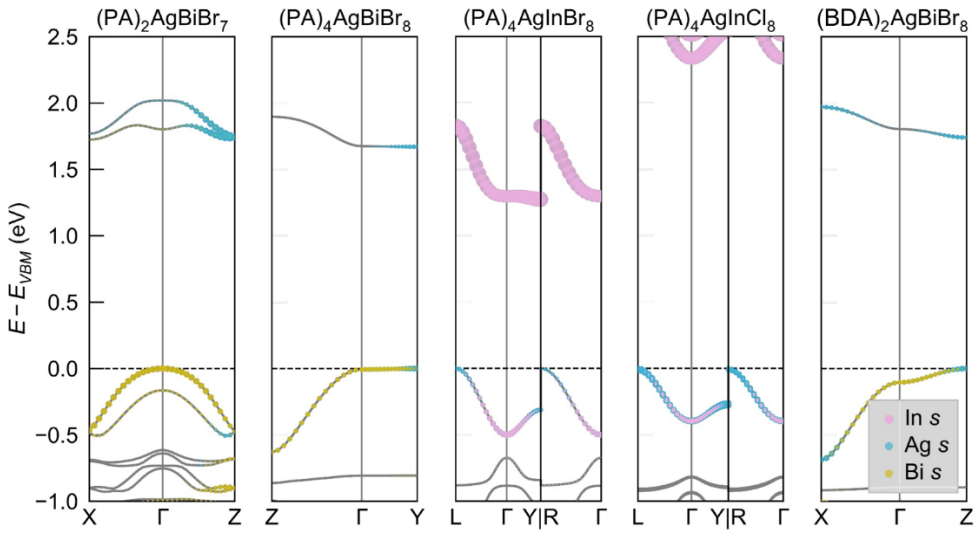

Figure S6. Zoom-in (x3) orbital projections of the VBMs and CBMs.

Section S5. X-ray Fluorescence (XRF) results

Table S5. Results of a spectroscopic scan of $PA_4AgSb_{0.5}Bi_{0.5}Br_8$ using a Rigaku ZSX Primus IV wavelength-dispersive X-ray fluorescence spectrometer. Spectroscopic lines for all elements with atomic numbers between 9 (F) and 92 (U) were considered. The converted atomic molar ratio of Bi and Sb is 0.4 and 0.6 (with respect to the ideal 0.5, 0.5). The organic part is not taken into account.

No.	Component	Result	Unit	Det. limit	El. line	Intensity	w/o normal
1	Br	67.0	mass%	0.32137	Br-KA	4.4992	45.7018
2	Ag	14.9	mass%	0.04597	Ag-KA (FA)	0.2834	10.1864
3	Bi	9.75	mass%	0.03384	Bi-LA (FA)	0.2328	6.6509
4	Sb	8.35	mass%	0.12162	Sb-KA (FA)	0.0975	5.6977

Table S5. Results of a spectroscopic scan of $PA_4AgIn_{0.5}Bi_{0.5}Br_8$ using a Rigaku ZSX Primus IV wavelength-dispersive X-ray fluorescence spectrometer. Spectroscopic lines for all elements with atomic numbers between 9 (F) and 92 (U) were considered. The converted atomic molar ratio of Bi and In is 0.6 and 0.4 (with respect to the ideal 0.5, 0.5). The organic part is not taken into account.

No.	Component	Result	Unit	Det. limit	El. line	Intensity	w/o normal
1	Br	68.4	mass%	0.01268	Br-KA (FA)	32.3891	70.0870
2	Ag	13.7	mass%	0.02426	Ag-KA (FA)	1.6837	14.0820
3	Bi	12.5	mass%	0.02143	Bi-LA (FA)	2.0745	12.7828
4	In	5.35	mass%	0.01499	In-KA (FA)	0.5787	5.4821